# Role of anharmonicity in dictating the thermal boundary conductance across interfaces comprised of two-dimensional materials

Sandip Thakur[1] and Ashutosh Giri[1,*]

[1]*Department of Mechanical, Industrial, and Systems Engineering, University of Rhode Island, Kingston, RI 02881, USA*

(Dated: June 16, 2023)

# Abstract

Understanding the fundamental heat transport mechanisms across interfaces comprised of 2D materials is crucial for the further development of next generation of optoelectronic devices based on 2D heterostructures for which one of the main factors affecting the device performance is their poor thermal management. Here we use systematic atomistic simulations to unravel the influence of anharmonicity in dictating the thermal boundary conductance across graphene and $MoS_2$ based 2D/3D interfaces. Specifically, we conduct nonequilibrium molecular dynamics simulations on computational domains with graphene or $MoS_2$ layers encapsulated between crystalline or amorphous silicon leads across a wide temperature range (of 50 K – 600 K). We show that while the interfacial conductance across graphene/crystalline silicon interface demonstrates considerable temperature-dependence, the conductance across graphene/amorphous silicon interface has no significant temperature-dependence. In contrast, the thermal boundary conductance for the $MoS_2$-based heterostructures with both the crystalline and amorphous leads demonstrate no significant temperature-dependence. Our spectral energy density calculations along with our spectrally resolved heat flux accumulation calculations on the various interfaces show that anharmonic coupling across the entire vibrational spectrum as well as the strong hybridization of a broader spectrum of the flexural modes with substrate Rayleigh waves in graphene heterostructures give rise to the relatively higher and drastically different heat transport mechanisms across these interfaces as compared to the $MoS_2$-based heterostructures. Through these understandings, we show that one strategy to enhance heat conductance across 2D/3D interfaces is to increase the anharmonic coupling between the acoustic and optic modes in the 2D materials by inducing a stronger interaction strength with the substrates. Our findings elucidate the fundamental heat transfer mechanisms dictating thermal boundary conductances across 2D/3D interfaces and will be crucial for heat dissipation in the next-generation of optoelectronic devices where the utilization of 2D materials are becoming ubiquitous.


## INTRODUCTION

Combining the remarkable properties of layered 2D semiconductors with the advantages of bulk materials, 2D/3D heterostructures have garnered considerable interest in the past two decades both from fundamental physics as well as applicative standpoints. For instance, the integration of


* ashgiri@uri.edu

2D materials such as $MoS_2$ and graphene in field-effect transistors (FETs) provides an avenue for excellent electrostatic gate control performances[1–3] and can potentially extend the Moore's scaling law beyond the current silicon-based FETs.[4] This is possible because of the pristine interfaces associated with 2D heterostructures that form weak van der Waals interactions with the underlying layers, thus removing the constraints of lattice mismatch and the negative impact of dangling bonds that can lead to performance degradation in conventional FETs.[5] However, one of the main factors limiting the performance of nanoelectronics (such as FETs) that utilize 2D/3D heterostructures is the large thermal boundary resistance at the weak van der Waals interfaces that poses as a major challenge for their proper thermal management.[6–8] Therefore, one of the key challenges in incorporating 2D/3D heterostructures to impact 2D optoelectronics,[9] nanophotonics,[10] and next-generation computing technologies[11] is the comprehensive understanding of heat transfer mechanisms dictating thermal boundary conductance ($h_{\rm K}$) across 2D/3D interfaces.

Considerable amount of work in the past few years have been devoted in understanding $h_{\rm K}$ across interfaces comprised of 2D materials. Overall, both experimental and theoretical works have shown that $h_{\rm K}$ across these interfaces are in the lower end of the spectrum for solid-solid interfaces mainly because of the weak interaction of the 2D layer with the underlying materials.[6, 12] Experimentally, Raman spectroscopy,[7, 13, 14] pump-probe thermoreflectance,[15–17] $3\omega$ technique,[18, 19] and electrical thermometries[20, 21] have been utilized to report $h_{\rm K}$ in the range of $\sim$10 - 35 MW m$^{-2}$ K$^{-1}$ for various 2D/3D interfaces, which is equivalent to the resistance offered by $\sim$40-100 nm thick $SiO_2$ layer.[16, 17, 20, 22, 23]

To understand the microscopic mechanisms dictating the low thermal conductances associated with interfaces comprised of 2D materials, considerable amount of work have also focused on atomistic simulations[24–30] as well as analytical and theoretical framework developments.[8, 31–36] One of the major findings from these works is that $h_{\rm K}$ across dimensionally mismatched 2D/3D interfaces is mainly driven by the coupling between flexural modes of the 2D material and the longitudinal phonons in the underlying substrate.[8, 25, 33] For instance, Persson *et al.*[32, 33] derived a theoretical model for $h_{\rm K}$ by accounting for the strength of interaction between the 2D material and the substrate, and (in reasonable agreement with experiments) predicted the $h_{\rm K}$ to be $\sim$25 MW m$^{-2}$ K$^{-1}$ between a weakly coupled graphene/$SiO_2$ interface. Ong *et al.*[34] further modified this theoretical model by adding a superstrate (a top encapsulating layer), which led to an increase in the heat transfer efficacy across the graphene/$SiO_2$ interface (with a value of $h_{\rm K}$=105

MW $m^{-2}$ $K^{-1}$ at room temperature that is in excellent agreement with experimental results from Chen *et al.*[18]). This increase was ascribed to additional channels of heat transfer that arise due to the coupling of the low frequency flexural modes of the graphene with the Rayleigh phonon modes from the superstrate. Similarly, the importance of flexural modes was further highlighted by Correa *et al.,*[31] where the authors defined a heat flux across dimensionally mismatched interfaces by incorporating a phonon-substrate interaction rate and first-principles calculated phonon dispersion relations as input parameters in their model. By comparing the results for heterostructures based on $MoS_2$ and graphene, they showed that a better overlap between the flexural modes and the substrate vibrational density of states (DOS) along with a stronger adhesion between the 2D material and 3D substrate resulted in a higher $h_{\mathrm{K}}$ across the graphene interface as compared to the $MoS_2$ interface.[31] Furthermore, utilizing the similar methodology, Foss *et al.*[8] calculated $h_{\mathrm{K}}$ across six common 2D-materials and seven different substrates to highlight the role of the substrate properties such as mass density and sound speed that play an important role (along with the flexural modes of the 2D material) while considering the heat transfer efficacy across 2D/3D interfaces. Although these works have helped shed light on the microscopic dynamics dictating $h_{\mathrm{K}}$ across 2D material interfaces, a complete understanding of the spectrally resolved interfacial conductance (such as the role of anharmonic coupling in the 2D layer) for 2D/3D heterostructures is still missing.

Herein, through systematic atomistic simulations, we show that along with the importance of flexural modes and the strength of interaction between the 2D material and the 3D substrate, the intrinsic anharmonicity and the strength of coupling between the modes of the 2D material dictates the temperature-dependent $h_{\mathrm{K}}$ across the dimensionally mismatched 2D/3D interfaces. More specifically, by considering $MoS_2$ and graphene on amorphous or crystalline silicon leads, we show that one of the main reasons for the higher interfacial conductances across the graphene-based interfaces is from the better coupling of the acoustic modes with the optical modes in graphene as compared to $MoS_2$. Furthermore, through our nonequilibrium molecular dynamics (NEMD) simulations, we show that while the $h_{\mathrm{K}}$ across graphene/crystalline silicon interface demonstrates considerable temperature-dependence, $h_{\mathrm{K}}$ across graphene/amorphous silicon interface has no significant temperature-dependence. In comparison, the interfaces associated with $MoS_2$ do not demonstrate a temperature-dependence for either the crystalline or amorphous leads. This highlights the role of anharmonic scattering in the leads along with the anharmonicity of the 2D materials in dictating the $h_{\mathrm{K}}$ across 2D/3D interfaces. Moreover, our extensive analyses

based on NEMD simulations, spectrally resolved heat flux accumulation calculations, and spectral energy density (SED) calculations demonstrate that the intrinsic anharmonicity of the 2D material dictates the efficacy of the flexural modes to couple with the phonon modes across the van der Waals interfaces. This intrinsic anharmonicity can be manipulated by varying the strength of interaction between the 2D material and the leads to drastically improve the heat transfer efficacy across even $MoS_2$-based interfaces that are typically associated with large thermal boundary resistaces ($1/h_{\mathrm{K}}$).

## METHODS

We perform MD simulations to predict and understand $h_{\mathrm{K}}$ across $MoS_2$ and graphene on amorphous or crystalline silicon substrates under the NEMD framework. For all our simulations, we utilize the large-scale atomic/molecular massively parallel simulator (LAMMPS) package.[37] We implement the Stillinger-Weber (SW) potential[38] to describe the interatomic interactions of the atoms in the $MoS_2$ layers. For the carbon atoms in the graphene layers, we utilize the Adaptive Intermolecular Reactive Empirical Bond-Order (AIREBO) potential,[39] which has been utilized to study the thermal properties of graphene.[40–42] For the Si atoms, the Tersoff potential[43] is used since it has been used previously to study thermal conductivities of both amorphous and crystalline silicon domains.[44–46] The SW potential for $MoS_2$ has also been used in prior literature to study their thermal as well as mechanical properties.[38, 47, 48] To model the interactions between the 2D monolayer and the 3D substrate, we use the Lennard-Jones (LJ) potential, which is given as,[49]

$$U = \sum_{i,j} 4\epsilon_{ij} \left[ \left( \frac{\sigma_{ij}}{r_{ij}} \right)^{12} - \left( \frac{\sigma_{ij}}{r_{ij}} \right)^{6} \right]. \tag{1}$$

Here $\epsilon_{ij}$ and $\sigma_{ij}$ are the characteristic parameters of energy and distance, respectively. The parameters for the different interactions are chosen based on the widely used Universal Force-Field.[49] Further details regarding the simulations and specific parameters for the LJ potential are given in the Supplemental Material.[50]

Initially the structures are equilibrated under the Nosé-Hoover thermostat and barostat (i.e. the NPT ensemble)[51] for 2 ns with a timestep of 0.5 fs where the number of particles, pressure and temperature of the system are held constant at 0 bar pressure. Following the NPT integration, further equilibration is carried out under the NVT ensemble where the volume and temperature

are kept constant for a total of 1 ns with periodic boundary conditions for the entire simulation. An additional equilibration is performed under NVE ensemble for 1 ns where number of particles, volume and total energy of the system are maintained constant.

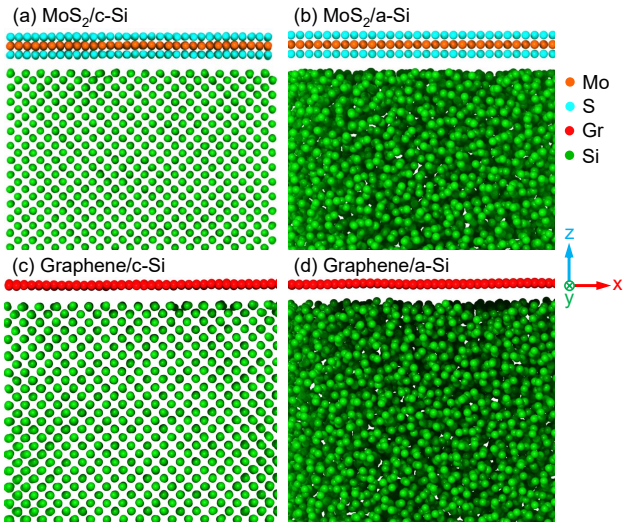


Figure 1. Schematic illustrations of parts of our computational domains for (a) $MoS_2$/c-Si, (b) $MoS_2$/a-Si, (c) graphene/c-Si, and (d) graphene/a-Si structures used for our atomistic simulations. Note, the schematics are only showing part of the domains to highlight the different interfaces studied in this work. We perform our calculations on structures with the 2D material encased between two semi-infinite silicon leads.

Figure 1 shows the schematic representations of parts of our equilibrated computational domains for our $MoS_2$ and graphene monolayers supported on crystalline silicon (c-Si) and amorphous silicon (a-Si) substrates. Even though we have only shown part of our computational domains (clearly showing the 2D/3D interfaces) in Fig. 1, we note that our NEMD simulations are carried out on sandwiched 2D structures that are encased between two semi-infinite leads. The leads are considered as semi-infinite because their prescribed lengths do not affect our predictions of $h_{\mathrm{K}}$ across the different 2D/3D interfaces. To make the amorphous Si substrates, we use the melt-quench technique[52–54] where a crystalline Si domain is initially melted at 4000 K, followed by rapid quenching to form an amorphous Si substrate. The structure is then allowed to equilibrate under the Nosé Hoover thermostat and barostat,[51] which is the NPT ensemble (with number of atoms, pressure and temperature held constant) for a total of 1 ns at a prescribed temperature and ambient pressure conditions.

To determine $h_{\mathrm{K}}$ across our 2D/3D interfaces, we implement the NEMD method where we impose a heat flux, $q$, across the equilibrated computational domain in order to establish a steady-state

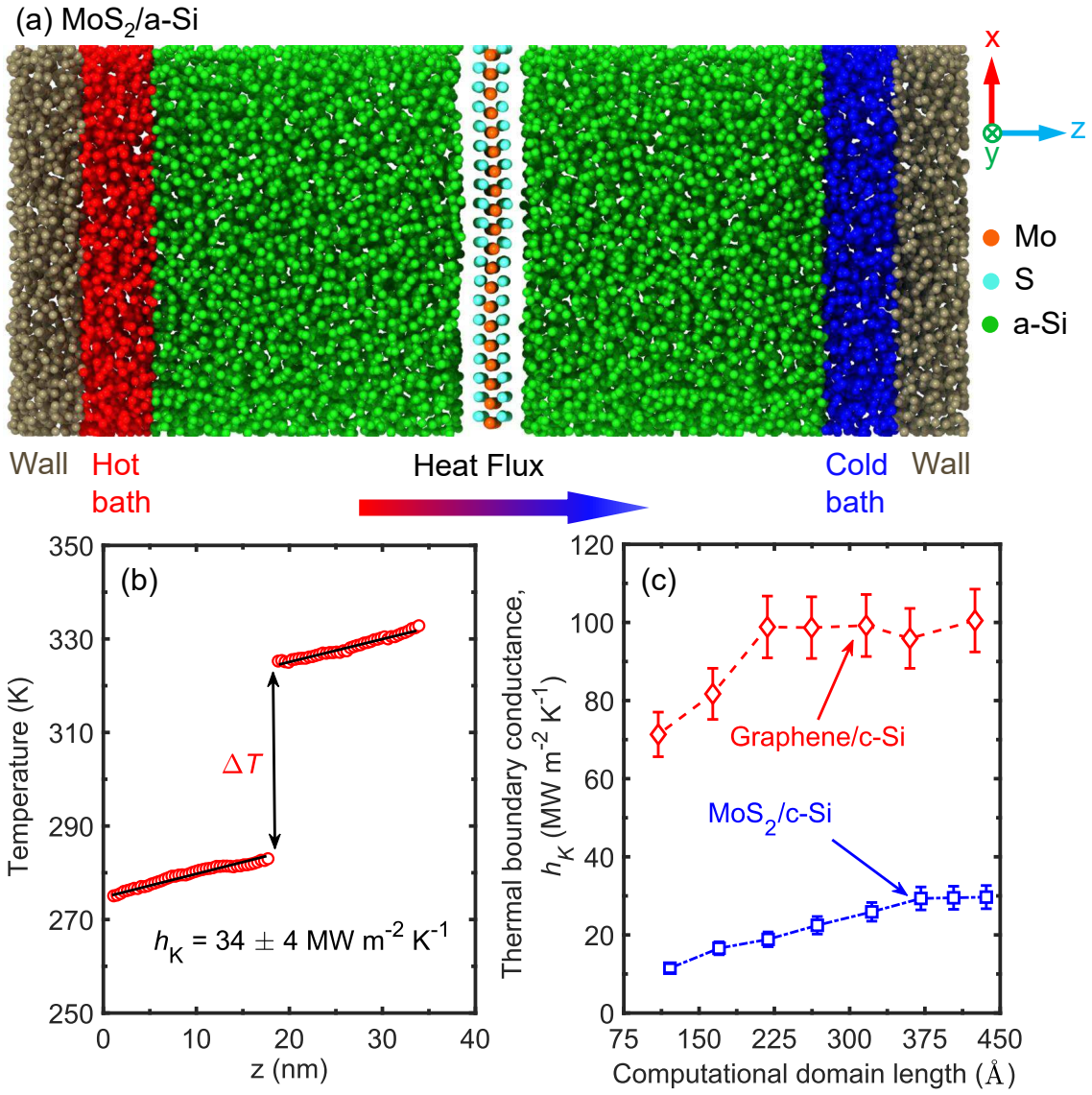


Figure 2. (a) Schematic illustration of the computational domain for our $MoS_2$/a-Si structure used in our NEMD simulations to predict the thermal boundary conductance across $MoS_2$/a-Si interface. (b) Steady-state temperature profile obtained from our NEMD simulation, which we utilize to calculate the thermal boundary conductance across $MoS_2$/a-Si interface. (c) NEMD simulations-predicted $h_K$ as a function of computational domain length (by varying the lengths of the silicon leads) for $MoS_2$/c-Si and graphene/c-Si heterostructures. The $h_K$ values converge for domain sizes greater than ~225 Å and ~375 Å for our graphene/c-Si and $MoS_2$/c-Si structures, respectively.

spatial temperature gradient as shown in Fig. 2 for our characteristic a-Si/$MoS_2$ heterostructure. This is carried out by prescribing a 'hot' region located at one end of the computational domain where we add energy at a constant rate and extracting the equal amount of energy from the 'cold'

region located at the other end of the computational domain. We partition our computational domain into different regions along the $z$-direction as shown in Fig. 2a, where the atoms in the 'wall' region are held fixed, while a fixed amount of heat is added and removed from the atoms in the 'hot bath' and 'cold bath' regions, respectively. Note, the 'wall' and the 'bath' regions are each $\sim$20 Å thick. In order to create a steady-state temperature profile across the $z$-direction of our computational domains, we apply a heat flux ($q$ = 0.8 GW m$^{-2}$) by adding a constant amount of kinetic energy (2.3 $\times$ 10$^{-5}$ J s$^{-1}$) to the 'hot' region and removing the equal amount of energy from the 'cold' region. For the temperature profiles, we divide the atoms in the computational domain into 100 equally sized bins along the direction of the applied heat flux. The temperature of the atoms in each bin is averaged after achieving steady-state, which results in a temperature profile as shown in Fig. 2b for the case of our $MoS_2$/a-Si domain. Finally, after we obtained a steady-state temperature profile, the $h_{\mathrm{K}}$ is calculated through the relationship given as,

$$h_{\mathrm{K}} = \frac{q}{\Delta T}. \tag{2}$$

Here $\Delta T$ is the temperature difference across 2D/3D interface, which is determined from the temperature profiles.

To ensure our results are not influenced by the size of our computational domains, we carried out a series of NEMD simulations by varying the length of the silicon leads in our simulation domain with total domain lengths of $\sim$110 Å to $\sim$436 Å along the direction of the applied heat flux as shown in Fig. 2c. The convergence of thermal boundary conductance within uncertainties for computational domain sizes greater than $\sim$225 Å and $\sim$375 Å for our graphene/c-Si and $MoS_2$/c-Si structures, respectively, ensures that our choice of the domain sizes do not influence our NEMD-predicted $h_{\mathrm{K}}$ values for both the $MoS_2$- and graphene-based heterostructures. The uncertainties in our reported $h_{\mathrm{K}}$ values are determined from five independent simulations along with the 95$\%$ confidence intervals based on fitting the temperature profiles of the silicon leads to obtain the temperature drops at the 3D/2D/3D interfaces.

We calculate the phonon mode specific properties of our unconstrained and encapsulted 2D structures in between the semi-infinite leads by utilizing the SED formalism. In this technique, the atomic motion trajectories are Fourier transformed to get the average kinetic energy per unit cell

at a specific wavevector ($\boldsymbol{k}$) and frequency ($\omega$), which is calculated as,[55, 56]

$$\Phi(\boldsymbol{k},\omega) = \frac{1}{4\pi\tau_0 N_T}\sum_{\alpha}^{3}\sum_{j}^{B} m_j \left| \int_0^{\tau_0} \sum_{n_{x,y,z}}^{N_T} \dot{u}_\alpha \begin{pmatrix} n_{x,y,z} \\ j \end{pmatrix}; t \right) \times exp\left[ i\boldsymbol{k}\cdot\boldsymbol{r}\begin{pmatrix} n_{x,y,z} \\ 0 \end{pmatrix} - i\omega t \right] dt \right|^2 . \quad (3)$$

Here $\tau_0$ is the total simulation time, $N_T$ is the number of unit cells in the crystal, $\alpha$ is the cartesian direction, $B$ is the atomic number in the unit cell, $j$ is the atom label in a given unit cell, $m_j$ is the mass of $j^{th}$ atom in the unit cell, $n_{x,y,z}$ is a unit cell, $\dot{u}_\alpha$ denotes the velocity along the $\alpha$ direction at time $t$ and $\boldsymbol{r}$ is the equilibrium position of each unit cell.

To ensure a high resolution in our SED calculations, we construct a larger simulation domain ($\sim$45$\times$6 nm$^2$ in the $x$ and $y$ directions) and extract 75 $k$-points along the $\Gamma$ to M direction. We equilibrate our supercell structure initially under the Nosé-Hoover thermostat and barostat[51] for 2 ns with a timestep of 0.5 fs where the number of particles, pressure and temperature of the system are held constant at 0 bar pressure. Following the NPT integration, further equilibration is carried out under the NVT ensemble for another 2 ns. Finally, for the data collection for our SED calculation, we output the velocities and positions of each atoms using the microcanonical ensemble (or NVE ensemble) for 1.5 ns.

To quantify the contributions of the specific vibrational frequencies to the total heat flow across the 2D/3D interfaces, we calculate the spectral heat flux accumulation that is given as,[57, 58]

$$Q = \int_0^\infty \frac{d\omega}{2\pi} q(\omega). \quad (4)$$

Here, $\omega$ is the angular frequency and $q(\omega)$ is the spectral heat current. This heat current is proportional to the correlation between the interatomic force between the atoms across the interface and the velocities,

$$q_{i\rightarrow j}(\omega) \propto \langle \overrightarrow{F}_{i,j} \cdot (\overrightarrow{v}_i + \overrightarrow{v}_j) \rangle. \quad (5)$$

Here the spectral heat current between atoms *i* and *j* is proportional to the correlation between the force of two atoms, $\overrightarrow{F}_{i,j}$ and their velocities, $\overrightarrow{v}_i$ and $\overrightarrow{v}_j$. For spectral heat flux accumulation calculations we collected the atomic forces and velocities for a total of 1 ns at a sampling interval of 5 fs. Further details of the spectral heat flux calculations are given in our prior work in Ref. 58.

## RESULTS AND DISCUSSION

Figure 3 shows our calculated temperature-dependent $h_K$ values for our 2D/3D interfaces across the temperature range of 50-600 K. Our predicted $h_K$ values of ~29 MW m$^{-2}$ K$^{-1}$ and ~34 MW m$^{-2}$ K$^{-1}$ for monolayer $MoS_2$ sandwiched between crystalline and amorphous leads, respectively, agree well with prior results.[13, 59] For instance, Gabourie *et al.*[59] report a value of $h_K$ = ~34.3 MW m$^{-2}$ K$^{-1}$ for $MoS_2$ on $Al_2O_3$ substrate at room temperature with an approach to equilibrium MD method. Yalon *et al.*[13] experimentally measured a value of $h_K$ = 14±4 MW m$^{-2}$ K$^{-1}$ at room temperature for $MoS_2$ encased between an $AlO_x$ layer and a $SiO_2$/Si substrate using Raman thermometry. Similarly, for our graphene/c-Si interface, we predict $h_K$ ~98 MW m$^{-2}$ K$^{-1}$, which is in good agreement with the experimentally determined value of ~83 MW m$^{-2}$ K$^{-1}$ for graphene/$SiO_2$ interface.[18] The slight discrepancies between the prior results and our MD results might arise due to the varying substrates, which (as we discuss below) can have a major influence on the interfacial conductance across 2D/3D interfaces.

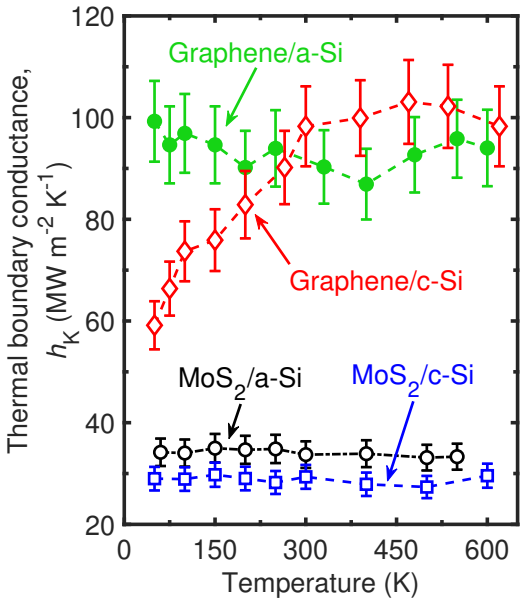


Figure 3. Nonequilibrium molecular dynamics simulations-predicted thermal boundary conductances ($h_K$) as a function of temperature for $MoS_2$/c-Si, $MoS_2$/a-Si, graphene/c-Si, and graphene/a-Si heterostructures. The $h_K$ across the 2D/3D interfaces are derived from structures where the 2D material is encapsulated between two semi-inifnite leads. The increasing trend in $h_K$ with temperature for the graphene/c-Si interface suggests that anharmonic scattering largely dictates the $h_K$ across this interface.

As shown in Fig. 3, the $h_K$ values predicted for both the $MoS_2$/c-Si and $MoS_2$/a-Si interfaces

show no temperature dependencies across the entire temperature range. In contrast, the graphene-based interfaces demonstrate drastically different thermal characteristics where the $h_{\mathrm{K}}$ across the graphene/c-Si interface shows considerable temperature-dependence, whereas the $h_{\mathrm{K}}$ across the graphene/a-Si interface is temperature-independent. These drastically different temperature trends for the $MoS_2$- and graphene-based interfaces show that the fundamental heat transfer mechanisms dictating $h_{\mathrm{K}}$ across these interfaces are characteristically different. For instance, the increasing $h_{\mathrm{K}}$ across the graphene/c-Si suggests that anharmonic interactions are more prevalent for this interface as compared to the others. Furthermore, the fact that replacing the crystalline leads with amorphous systems results in the lack of temperature-dependence of $h_{\mathrm{K}}$ indicates that anharmonic interactions in the leads (and not just limited to the 2D layer) also dictates the $h_{\mathrm{K}}$ across the graphene-based interfaces. In the amorphous leads, disorder scattering dominates over anharmonic scattering, which ultimately influences the temperature-dependence (or the lack there-of) for the $h_{\mathrm{K}}$ across graphene/a-Si interface. However, it is surprising that even for the $MoS_2$/c-Si interface we observe a similar temperature-dependence as the $MoS_2$/a-Si interface. Again, the lack of temperature-dependence for the $MoS_2$-based heterostructures indicates the lack of anharmonic scattering in dictating the interfacial conductance for these systems.

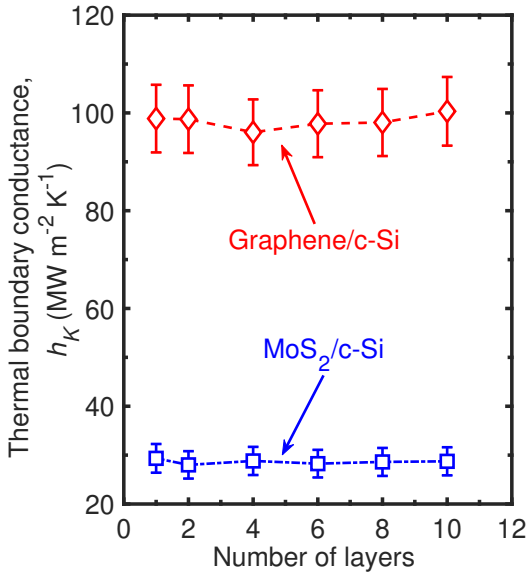


Figure 4. Calculated $h_{\mathrm{K}}$ as a function of the number of $MoS_2$ and graphene layers in our $MoS_2$/c-Si and graphene/c-Si heterostructures, respectively. For both the $MoS_2$/c-Si and graphene/c-Si heterostructures, we observe negligible influence on the thermal boundary conductance with the increase in the number of 2D layers.

Figure 4 shows the calculated thermal boundary conductance as a function of the number of layers for our $MoS_2$/c-Si and graphene/c-Si structures. For both the $MoS_2$/c-Si and graphene/c-Si heterostructures, the $h_K$ values do not significantly change with the increase in the number of 2D layers. The similarity in the $h_K$ values shows that the number of 2D layers has negligible influence in dictating the thermal boundary conductance across our 2D/3D interfaces.

As MD simulations are strictly classical in nature, all of the vibrational modes in the entire vibrational spectrum are activated at all temperatures. Thus, an increasing trend in $h_K$ with temperature is indicative of the prevalence of anharmonic effects.[57, 58, 60, 61] Therefore, although we cannot separate the contributions from harmonic and anharmonic processes in our NEMD simulations, the drastically different (and increasing) temperature dependence of graphene/c-Si interface signifies that inelastic processes are more prominent for this interface. However, we note that comparison to results from Atomistic Green's Function (AGF) calculations could lend more insights into the competing effects between elastic and inelastic processes,[62, 63] which is beyond the scope of the current work but deserves further attention.

The $h_K$ values predicted for the amorphous leads in the $MoS_2$-based structures are consistently higher for the entire temperature range when compared to the crystalline leads. Moreover, $h_K$ values predicted for graphene/a-Si interface are higher as compared to the $h_K$ for graphene/c-Si structure at lower temperatures below 300 K. These results are consistent with prior works where $h_K$ is reported to be higher for amorphous substrates as compared to the perfectly crystalline substrates.[64, 65] This has been attributed to better vibrational coupling of the heat carrying phonons across the disordered interfaces. Furthermore, in contrast to the $MoS_2$-based systems, the $h_K$ values across the crystalline and amorphous leads for our graphene-based heterostructures are similar within uncertainties at higher temperatures ($>$ 300 K). The slightly lower $h_K$ for the graphene/a-Si structure might be a result of competing effects between anharmonic scattering and disorder scattering across the graphene/silicon interfaces. However, within uncertainties of our NEMD simulations, a clear difference between the values predicted for $h_K$ across graphene/c-Si and graphene/a-Si is not observed. Therefore, we cannot draw any meaningful conclusions as to the effect of disorder in the atomic arrangement of the substrates on $h_K$ across graphene/Si interfaces at higher temperatures. In this regard, a comparison to AGF calculations that only consider harmonic effects might be useful to separate the competing effects between disorder and anharmonic scattering. Although such calculations are beyond the scope of the current work, disentangling the effects of disorder scattering and anharmonic scattering across these interfaces

clearly deserves further attention. We will now attempt to better explain and gain more insights into these different $h_K$ trends through spectrally resolved heat flux accumulation and SED calculations, as we discuss in detail below.

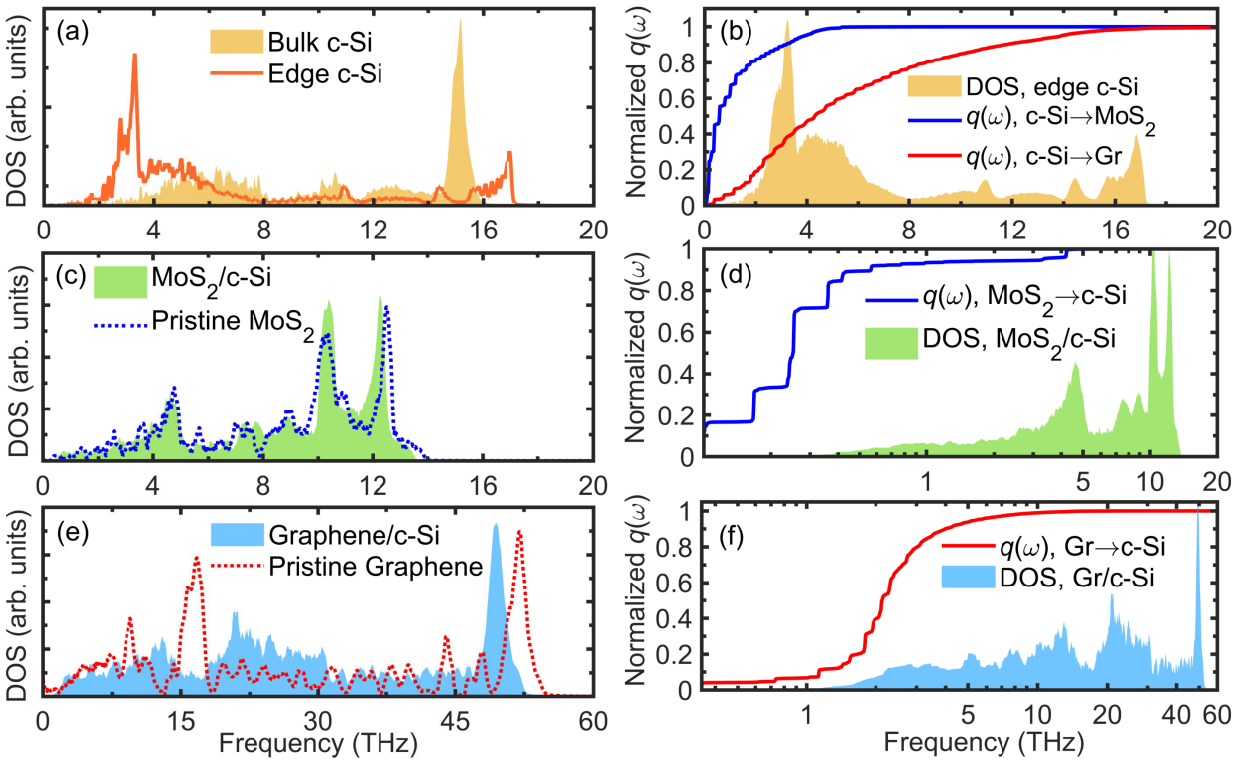


Figure 5. (a) Vibrational DOS and (b) spectrally resolved heat flux accumulation for monolayers of silicon atoms adjacent to the 2D materials. As compared to the DOS of the bulk silicon, frequencies in the 2-4 THz range have enhanced DOS for the interfacial monolayer of silicon atoms (edge c-Si). These modes are largely responsible for heat conduction across the interfaces to the adjacent 2D materials. The frequency range for transmission to the graphene layer is much broader in comparison to the $MoS_2$, which explains the higher $h_K$ values for the graphene/silicon interfaces. (c) Vibrational DOS and (d) spectrally resolved heat flux accumulation for $MoS_2$. The spectral region of flexural modes in $MoS_2$ that are responsible in carrying the heat across to the silicon leads is very narrow, which explains the higher thermal resistances associated with these interfaces. (e) Vibrational DOS and (f) spectrally resolved heat flux accumulation for graphene. Flexural modes as high as $\sim$10 THz can carry the heat across to the silicon leads, thus explaining their relatively higher values of $h_K$ as compared to the $MoS_2$-based interfaces.

Firstly, to understand the intrinsic mechanisms dictating the temperature-dependent $h_K$ values in these 2D/3D interfaces, we compare the vibrational density of states (DOS) and the spectrally

resolved heat flux accumulation calculations of the various systems in Fig. 5. As shown in Fig. 5a, we observe significant enhancement of DOS for vibrational frequencies in the 2-4 THz range for the monolayers of silicon atoms adjacent to the 2D materials as compared to the DOS of the bulk silicon atoms. As shown by our spectrally decomposed heat flux accumulation calculations in Fig. 5b for the heat flux from the silicon leads to the $MoS_2$ and graphene layers, the vibrational modes in this frequency range are largely responsible for coupling with the flexural modes of the 2D material to facilitate heat transport across the 2D/3D interface. It is also interesting to note that for the spectral heat flux across the silicon/graphene interface, the vibrational spectrum spans a much wider range as compared to the heat flux across the silicon/$MoS_2$ interface. This might not be surprising since the flexural ZA mode in graphene can span up to $\sim$15 THz.[66] This wider frequency spectrum responsible for heat conduction across the graphene-based interfaces also helps explain its stronger anharmonic nature as compared to the $MoS_2$-based interfaces. Moreover, when comparing the vibrational spectrum of the $MoS_2$ and graphene (Figs. 5c-f), it is evident that the stronger $sp^2$-bonded carbon atoms in the graphene layers results in a wider vibrational frequency spectrum. These higher frequency acoustic and optical modes in graphene might be responsible in dictating the anharmonic nature of the interfacial heat conduction. However, as shown by our heat flux accumulation calculations in Figs. 5d and 5f for $MoS_2$/c-Si and graphene/c-Si, respectively, the inefficient heat conduction across the 2D/3D interfaces, in general, can be attributed to the narrow frequency range capable of actually carrying the heat across these interfaces. Therefore, as shown by our calculations, and in agreement with prior results,[8, 25, 33, 67] the interfacial heat conduction across 2D/3D interfaces are categorically different as compared to 3D/3D interfaces since it is only through flexural modes that heat can couple across the 2D/3D interfaces. This is in contrast to the interfacial heat transport facilitated by impinging phonons undergoing a transmission or reflection at 3D/3D interfaces. As such, neither the DOS calculations nor the spectral heat flux calculations can provide a complete and clear picture of the intrinsic physical processes that result in the drastically different temperature-dependencies of $MoS_2$- and graphene-based interfaces.

To gain further insights into the intrinsic mechanisms dictating the heat transfer across our 2D/3D interfaces, we perform SED calculations.[55, 56] Figures 6a-d show the comparison of SEDs for the 2D materials with or without the leads (i.e. either encased or free-standing). This comparison will help elucidate the effect of encapsulation on the vibrational heat transport mechanisms across the interfaces. Note, the higher contrasts in the shading of the plots are related

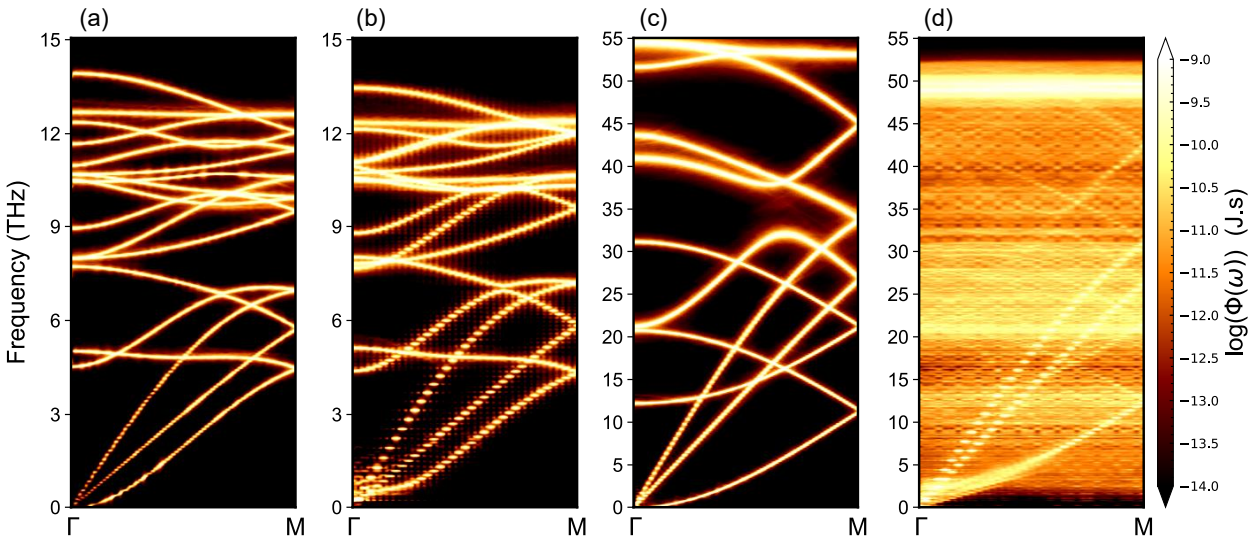


Figure 6. Calculated phonon spectral energy densities for (a) free-standing $MoS_2$ monolayer, (b) $MoS_2$/c-Si encased structure, (c) free-standing graphene monolayer, and (d) graphene/c-Si encased structure at room temperature. The relative effect on the anharmonicity of encapsulation for graphene in between the leads is much stronger where considerable broadening of the phonon branches is observed. This signifies enhanced vibrational coupling between the acoustic and optic modes in graphene-based heterostructures as compared to the $MoS_2$/c-Si encapsulated structure where we do not observe a significant increase in the broadening or change in the SEDs as compared to its free-standing counterpart.

to the higher magnitudes of the SEDs. Thus, the modes that appear brighter have higher kinetic energies. Also, the broadening of SEDs suggest larger anharmonicities, stronger scattering and reduced lifetimes of the phonon modes. For $MoS_2$ (Figs. 6a and 6b), the effect of encapsulation between the silicon leads on the SEDs is insignificant with minimal broadening of the vibrational modes. In contrast, for graphene (Figs. 6c and 6d), the effect of encapsulation between the leads is very evident where we observe significant broadening throughout the entire vibrational spectrum as compared to the SED of the free-standing structure suggesting considerable anharmonicities and vibrational coupling between the acoustic and optic modes when graphene is encased between the leads. This increase in anharmonicity and coupling of acoustic and optic modes results in the temperature-dependence and significantly higher $h_{\mathrm{K}}$ values for graphene/c-Si structure as compared to the $MoS_2$ structure. Moreover, as shown in Fig. 6d, the flexural (ZA) mode of graphene linearizes in the encapsulated case as compared to the unconstrained monolayer resulting in increased group velocities of the ZA modes. This enhancement in the group velocities and linearization of the ZA modes has been ascribed to the hybridization and coupling of graphene

ZA modes to the substrate Rayleigh waves.[24, 68] In fact, it has been shown that the hybridization between the substrate Rayleigh waves with the ZA modes in graphene leads to the reduction of the in-plane thermal conductivity.[68] However, when the strength of interaction between the substrate and graphene is increased, the thermal conductivity has been shown to increase due to enhanced coupling of the modes. We will draw similar conclusions on the effect of the strength of interaction on $h_{\mathrm{K}}$ as we discuss later.

The hybridization between the substrate Rayleigh waves and the flexural modes is considerably less prominent for the $MoS_2$ structure (Fig. 6b), which indicates that there are significantly less channels of heat conduction from the 2D layer to the leads. This is exemplified by the much weaker broadening of the very low frequency modes close to the Brillouin zone center in the encased $MoS_2$ (Fig. 6b) as compared to that in the encased graphene (Fig. 6d). Therefore, the $h_{\mathrm{K}}$ across $MoS_2$ interfaces are significantly lower than that of the anharmonic graphene interfaces (Fig. 3). Taken together, our SED calculations show that anharmonic coupling in the 2D material encapsulated between the leads can lead to higher transmission of vibrational energies through the hybridized ZA modes. As such, a viable route to increase the $h_{\mathrm{K}}$ across 2D/3D interfaces could be to increase the vibrational coupling within the 2D material itself.

To further increase the coupling of vibrational modes in the 2D material, we compress our computational domains along the direction normal to the 2D layers. Doing so, results in higher van der Waals interaction strengths between the 2D material and the leads, which has been linked to higher values of $h_{\mathrm{K}}$ across 2D/3D interfaces in prior works.[20, 67] Note, to determine the interlayer interaction strengths across our 2D/3D interfaces, we calculate the total pairwise interaction forces between the two groups of atoms (the first group consisting of the $MoS_2$ or the graphene monolayer and the second group consisting of a monolayer of silicon atoms adjacent to the 2D layer). The forces are averaged over a period of 0.5 ns in our simulations and the interaction strengths are normalized by the characteristic distance between the 2D layers and the 3D substrates. As shown in Fig. 7a, we also observe a monotonically increasing $h_{\mathrm{K}}$ across both the graphene and $MoS_2$ interfaces with increasing interaction strengths between the dimensionally mismatched interfaces. However, as expected, the graphene-based structures possess higher $h_{\mathrm{K}}$ values for the entire range of interaction strengths as compared to the $MoS_2$-based structures. More interestingly, we find that for $MoS_2$/c-Si computational domains with stronger interaction strengths, the NEMD-predicted $h_{\mathrm{K}}$ shows an increased temperature-dependence where $h_{\mathrm{K}}$ increases with increasing temperature as shown in Fig. 7b for the domain with the interaction strength of 34 N m$^{-1}$. This is in contrast to the

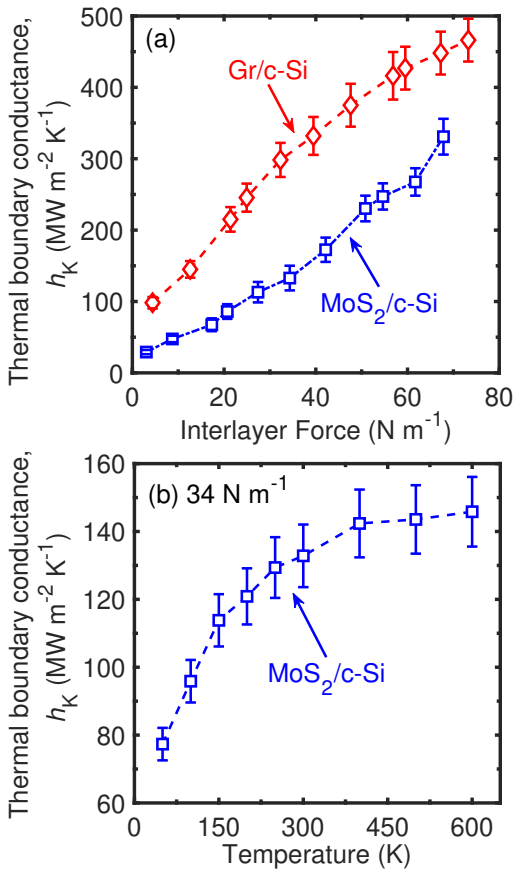


Figure 7. (a) Calculated thermal boundary conductances, $h_{\mathrm{K}}$ as a function of interlayer interaction strengths for $MoS_2$/c-Si and graphene/c-Si heterostructures. For both $MoS_2$/c-Si and graphene/c-Si interfaces, $h_{\mathrm{K}}$ increases monotonically with increasing van der Waals interaction strength. (b) NEMD-predicted $h_{\mathrm{K}}$ for $MoS_2$/c-Si structure showing an increased temperature-dependence when the interlayer interaction strength is increased to 34 N $\mathrm{m}^{-1}$. This suggests that increasing the van der Waals interaction strength between $MoS_2$ and silicon results in greater anharmonic interactions and therefore a greater temperature-dependence of $h_{\mathrm{K}}$ across the $MoS_2$/c-Si interface.

lack of temperature-dependence of the $h_{\mathrm{K}}$ for the uncompressed $MoS_2$/c-Si interface as shown in Fig. 3. This suggests that the $h_{\mathrm{K}}$ for the $MoS_2$/c-Si domains with higher van der Waals interaction strengths could largely be driven by enhanced anharmonic vibrational scattering mechanisms in the $MoS_2$ layer. These anharmonic processes could be a major factor in increasing the interfacial conductances for the highly thermally resistive $MoS_2$-based interfaces.

To support this hypothesis and to dig deeper into the intrinsic mechanism behind the temperature-dependent $h_{\mathrm{K}}$ in these materials, we further calculate the SEDs with increasing interlayer interaction strengths between the 2D/3D interfaces as shown in Fig. 8. For the $MoS_2$/c-Si struc-

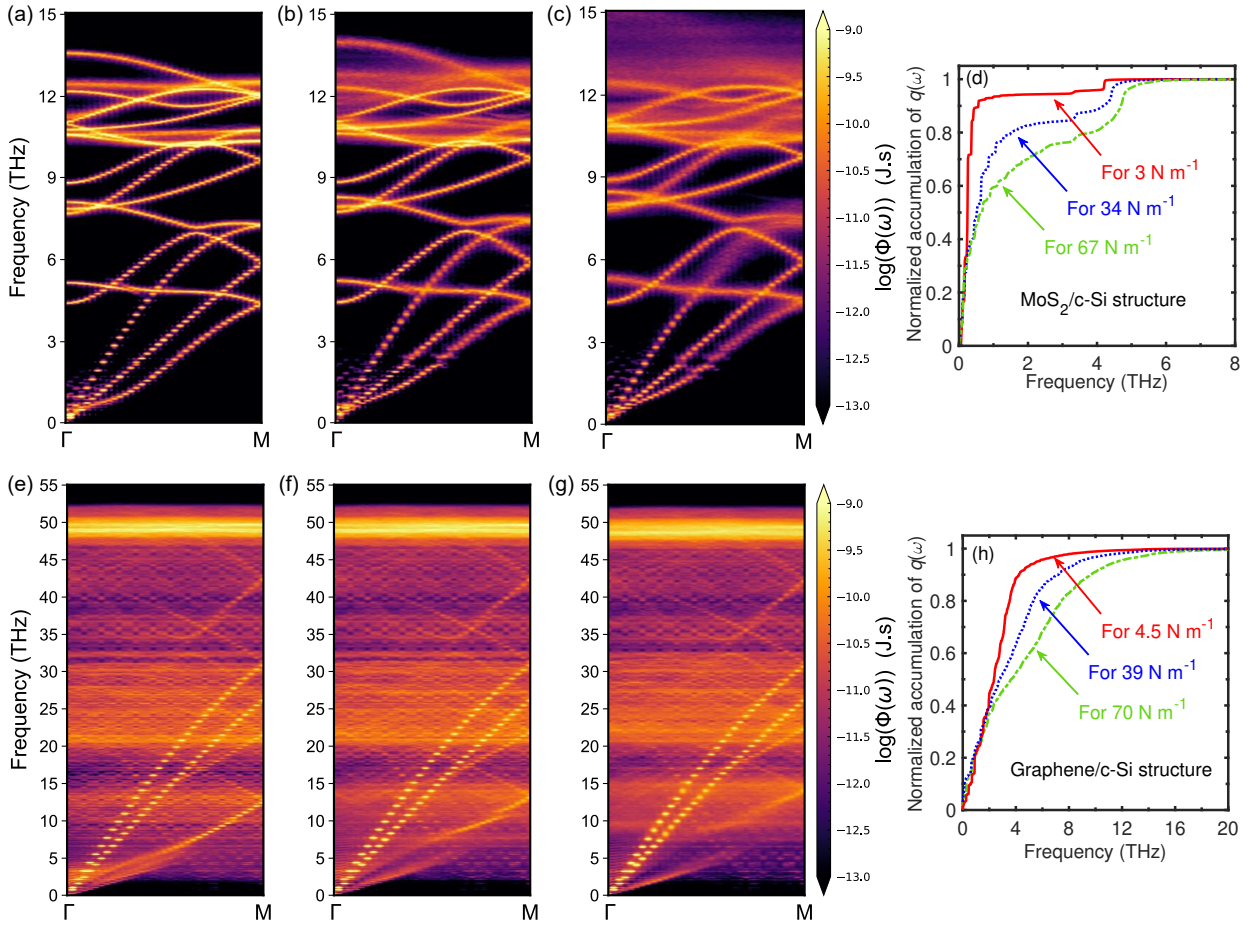


Figure 8. Calculated phonon spectral energy densities at room temperature for $MoS_2$/c-Si structure with (a) 5 N m$^{-1}$, (b) 34 N m$^{-1}$, and (c) 67 N m$^{-1}$ van der Waals interaction strengths. (d) Spectrally resolved heat flux accumulation for $MoS_2$ with varying interlayer interaction strengths. With increasing interaction strengths, the contribution to the interfacial conductance shifts to higher flexural frequencies. Calculated phonon spectral energy densities at room temperature for graphene/c-Si structure with (e) 6 N m$^{-1}$, (f) 39 N m$^{-1}$, and (g) 70 N m$^{-1}$ van der Waals interaction strengths. (h) Spectrally resolved heat flux accumulation for graphene with varying interlayer interaction strengths. Similar to the $MoS_2$ case, with increasing interaction strengths, the contribution to the interfacial conductance shifts to higher flexural frequencies. In-line with the spectral heat flux calculations, for the $MoS_2$/c-Si structure, we observe considerably increased anharmonicities with increase in the interlayer interaction strengths as evident from the broadening of the high frequencies optical and acoustic linewidths. Whereas, for the graphene system, although the increased anharmonicity is not so evident, the increased group velocities of the hybridized ZA modes lead to the monotonically increasing $h_K$ with increasing interaction strengths as shown in Fig. 7a.

ture (Fig. 8a-c), anharmonicity increases with increasing interlayer interaction strengths as evident from the increased broadening of the linewidths of the high frequency optical and acoustic branches. This suggests stronger coupling of the acoustic and optical modes in the $MoS_2$ layer leading to the higher values of $h_K$ with increasing interaction strengths as shown in Fig. 7a. Furthermore, the quadratic flexural mode also tends to linearize with increasing interaction strengths. In-line with our SED calculations, our spectrally resolved heat flux calculations show that the increasing van der Waals strength leads to an increase in the spectrum of flexural modes that are capable of carrying the heat across the 2D/3D interfaces (Fig. 8d). This is shown by the shift to higher frequencies of the contributions to the spectral heat flux across the $MoS_2$/c-Si interface with increasing interaction strengths. For the graphene-based systems (Fig. 8e-g), the increased effect of anharmonicity arising from the stronger interaction between the graphene and the leads is not so evident since the SEDs of the modes in the graphene-based domains already show pronounced anharmonicity even for the uncompressed structure. However, we do observe increasing group velocities of the hybridized ZA modes with increasing interaction strengths. Complementary spectrally decomposed heat flux accumulation also show a broader range of frequencies that are capable of transporting heat across the graphene/silicon interfaces (Fig. 8h). This increase in the frequency spectrum as well as the increased group velocities of the flexural modes explains the monotonically increasing $h_K$ of the graphene/c-Si interface as shown in Fig. 7a.

Our study reveals the fundamental mechanisms affecting the thermal boundary conductance across 2D material interfaces by utilizing systematic atomistic simulations. Our results have major implications on the interpretation of experimental results measuring $h_K$ across 2D/3D heterostructures that are ubiquitous in our current technology. For instance, 2D $MoS_2$ monolayers have been considered as novel channel materials for atomically thin transistors,[1] flexible electronics,[69] and opto-electronics.[70] However, experimental measurements have demonstrated ultralow values of $h_K$ across $MoS_2$ interfaces, which exposes the major thermal management issue originating at the 2D/3D interfaces in these devices. Our results presented in this work show that increasing the anharmonicity across these interfaces can drastically improve $h_K$, thus facilitating their proper thermal management and further advancements in the above-mentioned applications. Therefore, our results can help guide the proper thermal management in devices that incorporate 2D materials by increasing by increasing interfacial heat flow through strategically engineering the 2D/3D interfaces.

## CONCLUSIONS

In summary, we have performed systematic atomistic simulations on $MoS_2$- and graphene-based 2D/3D heterostructures to unravel the prominent role of anharmonic interactions in dictating their thermal boundary conductances. More specifically, by conducting NEMD simulations on $MoS_2$ or graphene that is encased between two semi-infinite leads of crystalline or amorphous silicon, we found that the graphene-based heterostructures demonstrated drastically higher anharmonic interactions that were significantly weaker in the $MoS_2$-based structures. Our SED calculations along with our spectrally decomposed heat flux accumulation calculations lend critical insights into the mode- and spectral-level details that dictate $h_{\mathrm{K}}$ across these 2D/3D interfaces. Through these analyses, we have shown that the stronger anharmonicity as well as a broader spectrum of flexural modes in graphene are responsible for almost four-fold higher interfacial conductances with a much more pronounced temperature-dependence as compared to $MoS_2$-based heterostructures. However, we have also shown that increasing the anharmonic interactions within the $MoS_2$ layer by increasing the van der Waals interaction strength with the 3D substrate can drastically enhance the interfacial conductances. Our results provide the fundamental understanding of the microscopic physical processes dictating interfacial heat flow across 2D material interfaces, and as such, will be critical for the further development of the next-generation of technologies utilizing 2D/3D heterostructures through their proper thermal management strategies.

## ACKNOWLEDGEMENTS

This work is supported by the Office of Naval Research, Grant No. N00014-21-1-2622. The work is also partially supported by the National Science Foundation (NSF Award No. 2119365).

---

[1] N. Li, Q. Wang, C. Shen, Z. Wei, H. Yu, J. Zhao, X. Lu, G. Wang, C. He, L. Xie, *et al.*, Large-scale flexible and transparent electronics based on monolayer molybdenum disulfide field-effect transistors, Nature Electronics **3**, 711 (2020).

[2] R. Cheng, J. Bai, L. Liao, H. Zhou, Y. Chen, L. Liu, Y.-C. Lin, S. Jiang, Y. Huang, and X. Duan, High-frequency self-aligned graphene transistors with transferred gate stacks, Proceedings of the National Academy of Sciences **109**, 11588 (2012).

[3] L. Britnell, R. Gorbachev, R. Jalil, B. Belle, F. Schedin, A. Mishchenko, T. Georgiou, M. Katsnelson, L. Eaves, S. Morozov, *et al.*, Field-effect tunneling transistor based on vertical graphene heterostructures, Science **335**, 947 (2012).

[4] R. J. Warzoha, A. A. Wilson, B. F. Donovan, N. Donmezer, A. Giri, P. E. Hopkins, S. Choi, D. Pahinkar, J. Shi, S. Graham, *et al.*, Applications and impacts of nanoscale thermal transport in electronics packaging, Journal of Electronic Packaging **143** (2021).

[5] T. Roy, M. Tosun, J. S. Kang, A. B. Sachid, S. B. Desai, M. Hettick, C. C. Hu, and A. Javey, Field-effect transistors built from all two-dimensional material components, ACS nano **8**, 6259 (2014).

[6] A. Giri and P. E. Hopkins, A review of experimental and computational advances in thermal boundary conductance and nanoscale thermal transport across solid interfaces, Advanced Functional Materials **30**, 1903857 (2020).

[7] E. Yalon, B. Aslan, K. K. Smithe, C. J. McClellan, S. V. Suryavanshi, F. Xiong, A. Sood, C. M. Neumann, X. Xu, K. E. Goodson, *et al.*, Temperature-dependent thermal boundary conductance of monolayer mos2 by raman thermometry, ACS applied materials & interfaces **9**, 43013 (2017).

[8] C. J. Foss and Z. Aksamija, Quantifying thermal boundary conductance of 2d–3d interfaces, 2D Materials **6**, 025019 (2019).

[9] Q. H. Wang, K. Kalantar-Zadeh, A. Kis, J. N. Coleman, and M. S. Strano, Electronics and optoelectronics of two-dimensional transition metal dichalcogenides, Nature nanotechnology **7**, 699 (2012).

[10] F. Xia, H. Wang, D. Xiao, M. Dubey, and A. Ramasubramaniam, Two-dimensional material nanophotonics, Nature Photonics **8**, 899 (2014).

[11] C. Liu, H. Chen, S. Wang, Q. Liu, Y.-G. Jiang, D. W. Zhang, M. Liu, and P. Zhou, Two-dimensional materials for next-generation computing technologies, Nature Nanotechnology **15**, 545 (2020).

[12] P. Hopkins, Isrn mechanical engineering, 2013, 2013 **682586**.

[13] E. Yalon, C. J. McClellan, K. K. Smithe, M. Muñoz Rojo, R. L. Xu, S. V. Suryavanshi, A. J. Gabourie, C. M. Neumann, F. Xiong, A. B. Farimani, *et al.*, Energy dissipation in monolayer $MoS_2$ electronics, Nano letters **17**, 3429 (2017).

[14] A. Behranginia, Z. Hemmat, A. K. Majee, C. J. Foss, P. Yasaei, Z. Aksamija, and A. Salehi-Khojin, Power dissipation of wse2 field-effect transistors probed by low-frequency raman thermometry, ACS applied materials & interfaces **10**, 24892 (2018).

[15] B. M. Foley, S. C. Hernandez, J. C. Duda, J. T. Robinson, S. G. Walton, and P. E. Hopkins, Modifying surface energy of graphene via plasma-based chemical functionalization to tune thermal and electrical

transport at metal interfaces, Nano letters **15**, 4876 (2015).

[16] P. E. Hopkins, M. Baraket, E. V. Barnat, T. E. Beechem, S. P. Kearney, J. C. Duda, J. T. Robinson, and S. G. Walton, Manipulating thermal conductance at metal–graphene contacts via chemical functionalization, Nano letters **12**, 590 (2012).

[17] Y. K. Koh, M.-H. Bae, D. G. Cahill, and E. Pop, Heat conduction across monolayer and few-layer graphenes, Nano letters **10**, 4363 (2010).

[18] Z. Chen, W. Jang, W. Bao, C. Lau, and C. Dames, Thermal contact resistance between graphene and silicon dioxide, Applied Physics Letters **95**, 161910 (2009).

[19] X. Li, Y. Yan, L. Dong, J. Guo, A. Aiyiti, X. Xu, and B. Li, Thermal conduction across a boron nitride and sio2 interface, Journal of Physics D: Applied Physics **50**, 104002 (2017).

[20] P. Yasaei, C. J. Foss, K. Karis, A. Behranginia, A. I. El-Ghandour, A. Fathizadeh, J. Olivares, A. K. Majee, C. D. Foster, F. Khalili-Araghi, *et al.*, Interfacial thermal transport in monolayer mos2-and graphene-based devices, Advanced Materials Interfaces **4**, 1700334 (2017).

[21] P. Yasaei, Z. Hemmat, C. J. Foss, S. J. Li, L. Hong, A. Behranginia, L. Majidi, R. F. Klie, M. W. Barsoum, Z. Aksamija, *et al.*, Enhanced thermal boundary conductance in few-layer ti3c2 mxene with encapsulation, Advanced Materials **30**, 1801629 (2018).

[22] J. Yang, E. Ziade, C. Maragliano, R. Crowder, X. Wang, M. Stefancich, M. Chiesa, A. K. Swan, and A. J. Schmidt, Thermal conductance imaging of graphene contacts, Journal of Applied Physics **116**, 023515 (2014).

[23] P. Yasaei, A. Behranginia, Z. Hemmat, A. I. El-Ghandour, C. D. Foster, and A. Salehi-Khojin, Quantifying the limits of through-plane thermal dissipation in 2d-material-based systems, 2D Materials **4**, 035027 (2017).

[24] Z.-Y. Ong, B. Qiu, S. Xu, X. Ruan, and E. Pop, Flexural resonance mechanism of thermal transport across graphene-sio2 interfaces, Journal of Applied Physics **123**, 115107 (2018).

[25] T. Feng, W. Yao, Z. Wang, J. Shi, C. Li, B. Cao, and X. Ruan, Spectral analysis of nonequilibrium molecular dynamics: Spectral phonon temperature and local nonequilibrium in thin films and across interfaces, Physical Review B **95**, 195202 (2017).

[26] Z. Xu and M. J. Buehler, Heat dissipation at a graphene–substrate interface, Journal of Physics: Condensed Matter **24**, 475305 (2012).

[27] H. Wang, J. Gong, Y. Pei, and Z. Xu, Thermal transfer in graphene-interfaced materials: contact resistance and interface engineering, ACS Applied Materials & Interfaces **5**, 2599 (2013).

[28] J. Zhang, Y. Hong, Z. Tong, Z. Xiao, H. Bao, and Y. Yue, Molecular dynamics study of interfacial thermal transport between silicene and substrates, Physical Chemistry Chemical Physics **17**, 23704 (2015).

[29] H. Zhang, H. Wang, S. Xiong, H. Han, S. Volz, and Y. Ni, Multiscale modeling of heat dissipation in 2d transistors based on phosphorene and silicene, The Journal of Physical Chemistry C **122**, 2641 (2018).

[30] S. V. Suryavanshi, A. J. Gabourie, A. Barati Farimani, and E. Pop, Thermal boundary conductance of two-dimensional $MoS_2$ interfaces, Journal of Applied Physics **126**, 055107 (2019).

[31] G. C. Correa, C. J. Foss, and Z. Aksamija, Interface thermal conductance of van der waals monolayers on amorphous substrates, Nanotechnology **28**, 135402 (2017).

[32] B. Persson, A. Volokitin, and H. Ueba, Phononic heat transfer across an interface: thermal boundary resistance, Journal of Physics: Condensed Matter **23**, 045009 (2011).

[33] B. Persson and H. Ueba, Heat transfer between graphene and amorphous sio2, Journal of physics: Condensed matter **22**, 462201 (2010).

[34] Z.-Y. Ong, Y. Cai, and G. Zhang, Theory of substrate-directed heat dissipation for single-layer graphene and other two-dimensional crystals, Physical Review B **94**, 165427 (2016).

[35] J. C. Duda, J. L. Smoyer, P. M. Norris, and P. E. Hopkins, Extension of the diffuse mismatch model for thermal boundary conductance between isotropic and anisotropic materials, Applied Physics Letters **95**, 031912 (2009).

[36] J. C. Duda, P. E. Hopkins, T. E. Beechem, J. L. Smoyer, and P. M. Norris, Inelastic phonon interactions at solid–graphite interfaces, Superlattices and Microstructures **47**, 550 (2010).

[37] S. Plimpton, Fast parallel algorithms for short-range molecular dynamics, Journal of computational physics **117**, 1 (1995).

[38] A. Kandemir, H. Yapicioglu, A. Kinaci, T. Çağın, and C. Sevik, Thermal transport properties of $MoS_2$ and $MoSe_2$ monolayers, Nanotechnology **27**, 055703 (2016).

[39] S. J. Stuart, A. B. Tutein, and J. A. Harrison, A reactive potential for hydrocarbons with intermolecular interactions, The Journal of chemical physics **112**, 6472 (2000).

[40] A. Giri and P. E. Hopkins, Resonant phonon modes in fullerene functionalized graphene lead to large tunability of thermal conductivity without impacting the mechanical properties, Journal of Applied Physics **125**, 205102 (2019).

[41] M. Noshin, A. I. Khan, I. A. Navid, H. A. Uddin, and S. Subrina, Impact of vacancies on the thermal conductivity of graphene nanoribbons: A molecular dynamics simulation study, AIP Advances **7**, 015112 (2017).

[42] C. Si, X.-D. Wang, Z. Fan, Z.-H. Feng, and B.-Y. Cao, Impacts of potential models on calculating the thermal conductivity of graphene using non-equilibrium molecular dynamics simulations, International Journal of Heat and Mass Transfer **107**, 450 (2017).

[43] S. Munetoh, T. Motooka, K. Moriguchi, and A. Shintani, Interatomic potential for Si–O systems using Tersoff parameterization, Computational Materials Science **39**, 334 (2007).

[44] P. K. Schelling, S. R. Phillpot, and P. Keblinski, Comparison of atomic-level simulation methods for computing thermal conductivity, Physical Review B **65**, 144306 (2002).

[45] J. M. Larkin and A. J. McGaughey, Thermal conductivity accumulation in amorphous silica and amorphous silicon, Physical Review B **89**, 144303 (2014).

[46] C. Abs da Cruz, K. Termentzidis, P. Chantrenne, and X. Kleber, Molecular dynamics simulations for the prediction of thermal conductivity of bulk silicon and silicon nanowires: Influence of interatomic potentials and boundary conditions, Journal of Applied Physics **110**, 034309 (2011).

[47] R. Xiang, T. Inoue, Y. Zheng, A. Kumamoto, Y. Qian, Y. Sato, M. Liu, D. Tang, D. Gokhale, J. Guo, *et al.*, One-dimensional van der waals heterostructures, Science **367**, 537 (2020).

[48] J.-W. Jiang, H. S. Park, and T. Rabczuk, Molecular dynamics simulations of single-layer molybdenum disulphide ($MoS_2$): Stillinger-Weber parametrization, mechanical properties, and thermal conductivity, Journal of Applied Physics **114**, 064307 (2013).

[49] A. K. Rappé, C. J. Casewit, K. Colwell, W. A. Goddard III, and W. M. Skiff, UFF, a full periodic table force field for molecular mechanics and molecular dynamics simulations, Journal of the American chemical society **114**, 10024 (1992).

[50] See Supplemental Material at [URL will be inserted by publisher] for universal force-field parameters for Lenard-Jones (LJ) potential used to model our 2D/3D interfaces; further details of non-equilibrium molecular dynamics simulations and vibrational density of states; schematic illustrations of the computational domains for our 2D/3D heterostructures; spectral energy density for crystalline silicon.

[51] W. G. Hoover, Canonical dynamics: Equilibrium phase-space distributions, Physical review A **31**, 1695 (1985).

[52] S. Thakur, C. J. Dionne, P. Karna, S. W. King, W. Lanford, H. Li, S. Banerjee, D. Merrill, P. E. Hopkins, and A. Giri, Density and atomic coordination dictate vibrational characteristics and thermal

conductivity of amorphous silicon carbide, Physical Review Materials **6**, 094601 (2022).

[53] A. Giri, C. J. Dionne, and P. E. Hopkins, Atomic coordination dictates vibrational characteristics and thermal conductivity in amorphous carbon, npj Computational Materials **8**, 55 (2022).

[54] A. Giri, P. E. Hopkins, J. G. Wessel, and J. C. Duda, Kapitza resistance and the thermal conductivity of amorphous superlattices, Journal of Applied Physics **118**, 165303 (2015).

[55] J. A. Thomas, J. E. Turney, R. M. Iutzi, C. H. Amon, and A. J. McGaughey, Predicting phonon dispersion relations and lifetimes from the spectral energy density, Physical Review B **81**, 081411 (2010).

[56] J. A. Thomas, J. E. Turney, R. M. Iutzi, C. H. Amon, and A. J. McGaughey, Erratum: Predicting phonon dispersion relations and lifetimes from the spectral energy density [Phys. Rev. B 81, 081411 (r)(2010)], Physical Review B **91**, 239905 (2015).

[57] K. Sääskilahti, J. Oksanen, J. Tulkki, and S. Volz, Role of anharmonic phonon scattering in the spectrally decomposed thermal conductance at planar interfaces, Physical Review B **90**, 134312 (2014).

[58] A. Giri, J. L. Braun, and P. E. Hopkins, Implications of interfacial bond strength on the spectral contributions to thermal boundary conductance across solid, liquid, and gas interfaces: A molecular dynamics study, The Journal of Physical Chemistry C **120**, 24847 (2016).

[59] A. J. Gabourie, Ç. Köroğlu, and E. Pop, Substrate-dependence of monolayer $MoS_2$ thermal conductivity and thermal boundary conductance, Journal of Applied Physics **131**, 195103 (2022).

[60] E. Landry and A. McGaughey, Thermal boundary resistance predictions from molecular dynamics simulations and theoretical calculations, Physical Review B **80**, 165304 (2009).

[61] P. E. Hopkins, J. A. Tomko, and A. Giri, Quasi-harmonic theory for phonon thermal boundary conductance at high temperatures, Journal of Applied Physics **131**, 015101 (2022).

[62] S. Sadasivam, Y. Che, Z. Huang, L. Chen, S. Kumar, and T. S. Fisher, The atomistic green's function method for interfacial phonon transport, Annual Review of Heat Transfer **17** (2014).

[63] N. Mingo and L. Yang, Phonon transport in nanowires coated with an amorphous material: An atomistic Green's function approach, Physical Review B **68**, 245406 (2003).

[64] M. Li, J. Zhang, X. Hu, and Y. Yue, Thermal transport across graphene/SiC interface: effects of atomic bond and crystallinity of substrate, Applied Physics A **119**, 415 (2015).

[65] Q. Wang, J. Zhang, Y. Xiong, S. Li, V. Chernysh, and X. Liu, Atomic-scale surface engineering for giant thermal transport enhancement across 2D/3D van der waals interfaces, ACS Applied Materials & Interfaces (2023).

[66] A. Ipatov, D. Parshin, and D. Conyuh, Dispersion of flexural modes in graphene, Journal of Experimental and Theoretical Physics **133**, 461 (2021).

[67] C. Foss and Z. Aksamija, Thermal boundary conductance of monolayer beyond-graphene two-dimensional materials on sio2 and gan, Nanotechnology **32**, 405206 (2021).

[68] Z.-Y. Ong and E. Pop, Effect of substrate modes on thermal transport in supported graphene, Physical Review B **84**, 075471 (2011).

[69] X. Li, L. Tao, Z. Chen, H. Fang, X. Li, X. Wang, J.-B. Xu, and H. Zhu, Graphene and related two-dimensional materials: Structure-property relationships for electronics and optoelectronics, Applied Physics Reviews **4**, 021306 (2017).

[70] A. Daus, S. Vaziri, V. Chen, Ç. Köroğlu, R. W. Grady, C. S. Bailey, H. R. Lee, K. Schauble, K. Brenner, and E. Pop, High-performance flexible nanoscale transistors based on transition metal dichalcogenides, Nature Electronics **4**, 495 (2021).